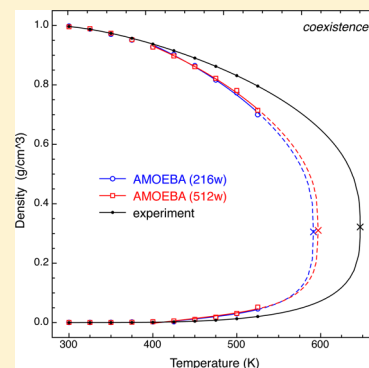


Water from Ambient to Supercritical Conditions with the AMOEBA Model

Daniel M. Chipman

Radiation Laboratory, University of Notre Dame, Notre Dame, Indiana 46556-5674, United States

ABSTRACT: The flexible polarizable AMOEBA force field for water is tested with classical molecular dynamics simulations from ambient up to supercritical conditions. Good results are obtained for the heat of vaporization, dielectric constant, self-diffusion constant, and radial distribution functions provided densities are fixed at the experimental values. If instead the densities are allowed to relax to those characteristic of the liquid–gas equilibrium for the model, then satisfactory results are obtained near ambient conditions, whereas at high temperatures the liquid densities are generally underestimated and the gas densities overestimated. As a consequence, the critical point of the model is reached at significantly too low temperature, although it occurs at approximately the correct density.



INTRODUCTION

The properties and reactions of radiolytic species in water from ambient up to supercritical conditions are of particular importance in the nuclear power industry.¹ While a substantial amount of information on this topic is available,² a number of important reactions have not been characterized at high temperatures because of experimental difficulties. Molecular simulations should therefore be useful in this context, and this is our long-range goal. As a first step, it is necessary to validate a force field that performs well for water itself under such a wide range.

Many force fields have been developed for classical molecular simulations involving condensed phase water, and several of these are now in widespread use.^{3–7} For computational efficiency, these force fields typically invoke pairwise interactions, with many-body effects represented only in some average manner by suitable adjustment of parameters in the model. While generally performing well at ambient conditions, such models may not be able to represent the properties of water over a wide range of thermodynamic conditions.⁸ With increases in computing power, it is now possible to treat true many-body effects either by inclusion of polarizability^{9–23} or by explicit representation of 3-body interactions.^{24–26} Several of these polarizable force fields have been tested at elevated temperatures and pressures.^{13,17,18,21,23,27–34}

The flexible polarizable AMOEBA model¹⁶ is of particular interest because its basic recipe has also been parametrized for many solutes and shown to be very successful in describing the behavior of a large variety of neutral organic,^{35–37} ionic inorganic,^{35,38–44} and biochemical³⁵ species in water. To date it has been validated only over a limited range of near-ambient temperatures and at high pressures,³⁰ and a recent study⁴⁵ indicates that it does not reproduce 2- and 3-body interactions completely accurately. The present work investigates the

performance of the AMOEBA force field for describing properties of water from ambient up to supercritical conditions. We evaluate the heat of vaporization, dielectric constant, self-diffusion constant, radial distribution functions, and liquid–gas equilibrium densities. It is found that, with the notable exception of liquid–gas equilibrium densities at high temperatures, AMOEBA can indeed perform well under these conditions.

METHODS

The AMOEBA force field for water is described well in the literature,^{16,30,35} so we provide here only a brief summary without giving full numerical details. The flexible water monomer geometry and vibrational motions are described with an anharmonic force field including Urey–Bradley terms. Electrostatic interactions are governed by permanent charges, dipoles, and quadrupoles on each atom, and induced dipoles are allowed to further develop via polarizabilities assigned to each atom. The electrostatic and induction interactions use smeared multipoles to provide Thole-type⁴⁶ damping that prevents short-range polarization catastrophes. van der Waals terms for intermolecular dispersion and exchange repulsion are described with a buffered 14–7 potential on oxygen and at points on the OH bonds near the hydrogens. Properties of dimer through hexamer gas-phase water clusters as well as of bulk ambient water were considered while optimizing the various parameters.

Classical molecular dynamics simulations were carried out with the Tinker program⁴⁷ that was originally used to develop the AMOEBA model, adopting without change the original

Received: January 22, 2013

Revised: April 5, 2013

parameters of the model. Simulations were carried out at constant particle number and constant volume. In most cases, temperature was held nearly constant through velocity scaling regulated by the Berendsen weak-coupling thermostat.⁴⁸ This strictly gives an ensemble intermediate between canonical and microcanonical,⁴⁹ which with the default coupling time constant of 0.1 ps used in the calculations reported herein approaches closely the weak coupling limit of the canonical ensemble. Some spot checks on the self-diffusion constant were made by comparing to calculations carried out in the microcanonical ensemble.

Cubic boxes containing either 216 or 512 water molecules were considered. In most cases, the box size was set to reproduce the experimental density, with the exception of one series of calculations where the boxes were extended in one direction to become rectangular in order to determine the liquid–vapor equilibrium. Periodic boundary conditions were invoked, using particle-mesh Ewald summation of order 8 for electrostatic interactions with a cutoff radius of 9 Å. The van der Waals interactions beyond 12 Å were tapered to zero with a 1.2 Å switching function. The equations of motion were integrated with a modified Beeman algorithm.^{50,51} Induced dipoles were converged to 10^{-4} D rms. At each state point the equilibration phase was run for at least 200 ps starting from a nearby state point, followed by a production run of 1 ns, using time steps of 1.0 fs. For the liquid–vapor equilibrium calculations, a longer equilibration phase of at least 500 ps was used.

High temperatures were considered up to and above the experimental critical point of water, which occurs at⁵² 647.1 K and 220.6 bar corresponding to a density of $\rho = 0.322$ g/cm³. A series of subcritical calculations was made along the liquid–vapor coexistence line varying the temperature from 300 up to 647.1 K. A separate series of supercritical calculations held the temperature fixed at 653 K and varied the pressure from 290 down to 210 bar. For reference, plots of the experimental densities⁵³ obtained under these conditions are given in Figure 1, where it is seen that the densities considered span a range from 0.997 down to 0.139 g/cm³. State points where simulations were carried out are marked with exaggerated dots in Figure 1, and also on the experimental curves displayed for other properties in subsequent figures.

The symbols used are V for volume, P for pressure, k for the Boltzmann constant, T for absolute temperature, ρ for density, K for kinetic energy, U for potential energy, $H = K + U + PV$ for enthalpy, ϵ for dielectric constant, M for vector dipole moment of the entire simulation box, and D for self-diffusion constant.

Heat of Vaporization. The enthalpy of vaporization is obtained from

$$\Delta H^{\text{vap}} = \langle U \rangle_{\text{gas}} - \langle U \rangle_{\text{liq}} + \langle PV \rangle_{\text{gas}} - \langle PV \rangle_{\text{liq}}$$

The difference in kinetic energy between the gas and liquid phase is omitted since in a classical simulation the kinetic energy is determined by the equipartition principle and so is essentially the same in the gas and liquid phases at any given temperature. It is commonplace to replace $\langle PV \rangle_{\text{gas}}$ by kT , which is entirely appropriate at ambient conditions, but that is not done here because intermolecular interactions cause the calculated nonideality of this quantity to be up to 0.8 kcal/mol at the highest temperatures considered. It is further commonplace to neglect $\langle PV \rangle_{\text{liq}}$ since it is negligible at ambient conditions, but this quantity is included here because it is

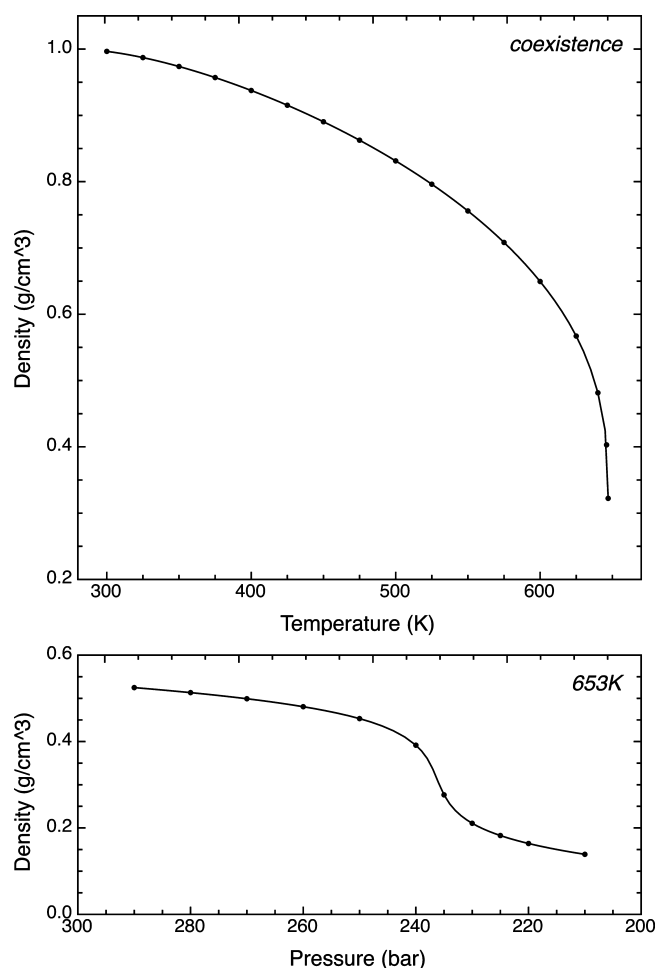


Figure 1. Experimental liquid water density vs temperature along the liquid–vapor coexistence line (upper panel) and vs pressure at fixed temperature of 653 K (lower panel). Exaggerated dots are placed at state points where simulations were carried out.

calculated to be up to 0.5 kcal/mol at the highest temperatures considered.

Contributions to the liquid-phase enthalpy were taken directly from the calculations in all cases, as were contributions to the gas-phase enthalpy for temperatures ≥ 500 K for the 216 water box case and ≥ 575 K for the 512 water box case. However, gas-phase calculations were not feasible at the lower temperatures because the large box sizes made the runs exorbitantly long. Reasonable estimates were therefore made to obtain the gas-phase enthalpy for the 216 water box case at the lower temperatures. The gas-phase enthalpy calculated in that case at 500 K was found to be only 0.5 kcal/mol lower than that for an ideal gas of classical flexible water molecules. Making an assumption that the gas is essentially ideal at 300 K, the gas-phase enthalpy between 300 and 500 K was then estimated for the 216 water box case to be the ideal result plus a nonideality correction ranging linearly between 0 at 300 K and -0.5 kcal/mol at 500 K. This linear interpolation estimate of the small nonideality correction should be in error by no more than ~ 0.1 kcal/mol over that range.

We note that the separate enthalpies calculated for gas and liquid phases would not compare well with experiment, because the simulation treats vibrations classically while the experiment reflects the actual quantized nature of the vibrations. However, this discrepancy cancels out to a large extent when taking the

difference between gas and liquid, and it is therefore meaningful to directly compare the calculated and experimental heats of vaporization. Even so, it should be kept in mind that this discrepancy means that even simulations carried out with a very accurate classical force field should not produce excellent agreement with experiment.⁵⁴ For example, it has been estimated⁸ that at 298 K the experimental heat of vaporization of 10.5 kcal/mol would become 11.0 kcal/mol for hypothetical classical water.

Results are compared with experiment⁵³ in Figure 2. The simulation results are shown with blue symbols where all

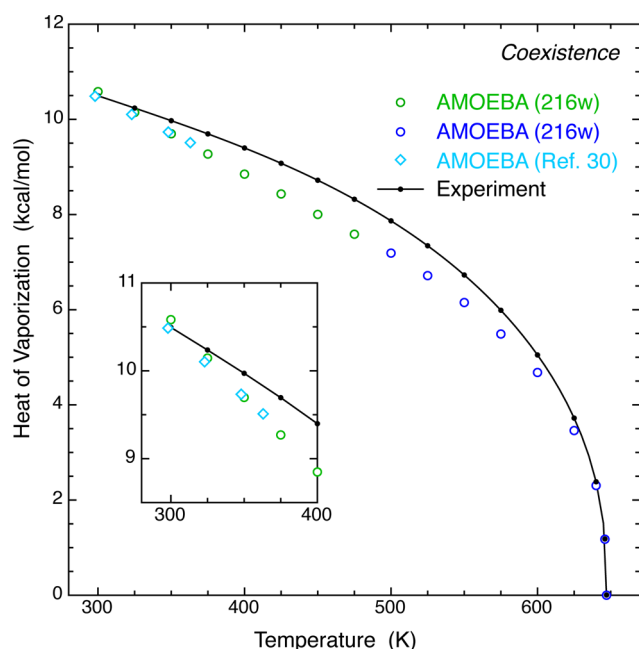


Figure 2. Heat of vaporization vs temperature along the liquid–vapor coexistence line. The dark blue symbol results obtain all contributions from the simulations, while the green symbol results invoke an estimate of the gas nonideality at the lower temperatures. Light blue symbols refer to previous results that assume gas ideality.

contributions were obtained from the simulations and with green symbols in the region where the gas-phase enthalpy nonideality was estimated instead of calculated. Statistical errors for the simulations, estimated from the potential energy fluctuations, are about the size of the symbols or smaller and so are not shown. The 512 water box results are not shown because on the scale of the figure they are essentially indistinguishable from the 216 water box results.

The present results agree well with a previous calculation made at the lower temperatures under the assumption of an ideal gas.³⁰ They are in very good agreement with experiment at 300 K, due in part to the fact that this property at ambient temperature was among the experimental data considered while optimizing the van der Waals parameters of the AMOEBA model.¹⁶ At higher temperatures the calculated results are lower and less curved than the experimental ones, but then come back into very good agreement with experiment on approaching near the critical point.

Dielectric Constant. The static dielectric constant is given under the simulation conditions used here by^{55–57}

$$\epsilon = 1 + \left(\frac{4\pi}{3V} \right) \text{Tr}(\mathcal{A}) + \left(\frac{4\pi}{3VkT} \right) (\langle M^2 \rangle - \langle M \rangle^2)$$

Here \mathcal{A} is the molecular electronic polarizability, and the term involving it along with the unity term comprise the high-frequency dielectric constant. The contribution calculated from the electronic polarizability term is generally small, ranging from up to 0.6 at ambient conditions down to as low as 0.1 at supercritical temperature and low density. The last term involving fluctuations of the dipole moment arises mainly from the orientational polarizability and makes the largest contribution to the total dielectric constant.

Results are compared with experiment⁵³ in Figure 3. Statistical errors for the simulations are estimated by a blocking

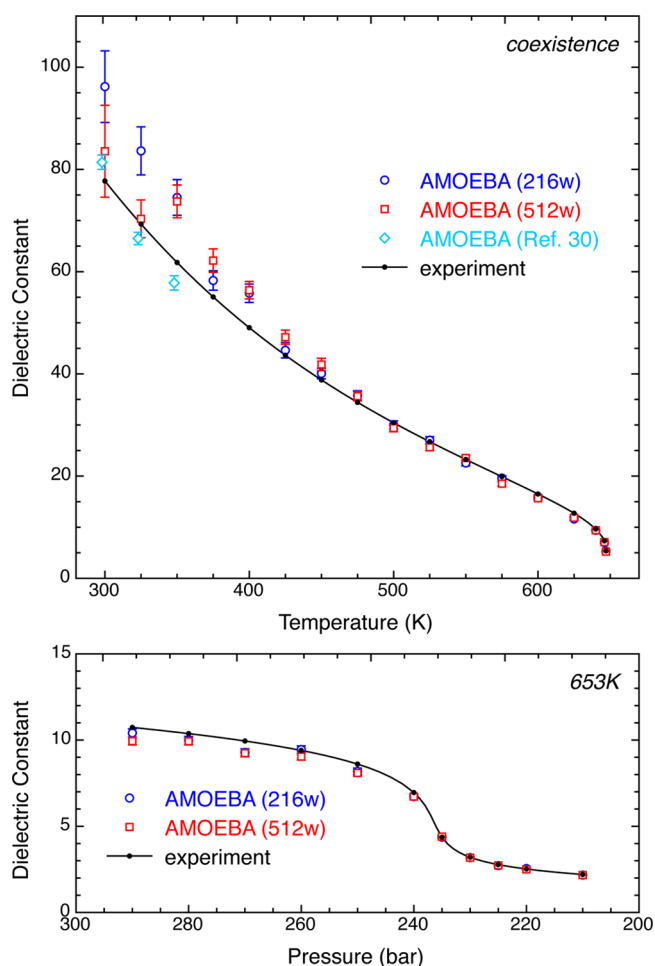


Figure 3. Dielectric constant of liquid vs temperature along the liquid–vapor coexistence line (upper panel) and vs pressure at fixed temperature of 653 K (lower panel).

procedure.⁵⁸ The dipole moment is a very slowly converging quantity,⁵⁹ which raises potential concerns about convergence. The small statistical errors in our results suggest good convergence in most cases, except for the run at 300 K where the large apparent statistical error might instead reflect a lack of convergence there. To check that possibility, another 1 ns run was made at 300 K for the 216 water simulation. That run led to a dielectric constant of 98.1, which is well within the range of 96.2 ± 5.6 shown for this case in Figure 3, thereby indicating that the error bars reported at 300 K, and presumably elsewhere as well, are mostly due to statistical fluctuations rather than to lack of convergence.

The upper panel of Figure 3 shows the liquid dielectric constant versus temperature along the liquid–vapor coex-

istence line. Statistical errors are large at the lower temperatures, where the simulations give results somewhat higher than experiment. At the lower temperatures, where comparison is possible, the present results are also somewhat higher than a previous calculation³⁰ that used a different computational protocol based on an isolated liquid droplet for this property, and which is probably more precise than the protocol used here for this property. As temperature increases, the statistical errors in the simulations become much smaller, and above about 425 K the agreement with experiment becomes excellent.

The lower panel of Figure 3 shows the dielectric constant versus pressure at the fixed supercritical temperature of 653 K. Even with the expanded scale, the statistical errors are smaller than the symbols on the graph and so are not shown. Overall agreement with experiment is quite good for both the 216 and 512 water simulations, and is excellent at the lower pressures.

Self-Diffusion Constant. The self-diffusion constant was evaluated from the Einstein relation

$$D = \frac{\langle [\mathbf{r}(t) - \mathbf{r}(0)]^2 \rangle}{6t}$$

where \mathbf{r} denotes the molecular center of mass, which relation is valid at large time t . The average here was taken over all molecules and over all time origins separated by 1 ps intervals, except that elapsed times of less than 20 ps were excluded.

Results are compared with experiment⁶⁰ in Figure 4. Statistical errors for the simulations are estimated as the standard deviation from the mean of the individual x -, y -, and z -components of the calculated self-diffusion constant. Dynamical properties such as the self-diffusion constant should more properly be evaluated in the microcanonical ensemble. To check whether our use of the Berendsen weak-coupling ensemble gives reasonable results for this property, we have carried out calculations using the microcanonical ensemble for the 216 water case at the ambient temperature of 300 K and the experimental critical temperature of 647.1 K. These spot checks produced self-diffusion constants agreeing with the ones reported here to within the estimated statistical errors, thereby validating use of the Berendsen weak-coupling ensemble for this property.

The upper panel of Figure 4 shows the liquid self-diffusion constant versus temperature along the liquid branch of the liquid–vapor coexistence line. For the most part the 216 and 512 water simulation results agree very well with one another and, at the lower temperatures where comparison is possible, fairly well with a previous calculation.³⁰ At 300 K the respective 216 and 512 water results are 1.58×10^5 and 1.70×10^5 cm²/s, which are 30% and 25% below the experimental value of 2.26×10^5 cm²/s. Part of this discrepancy can be attributed to our neglect of nuclear quantum effects. Recent calculations⁶¹ indicate nuclear quantum effects would increase the self-diffusion constant by about 15% at ambient conditions, although there is discussion about the accuracy of that result⁶² and other calculations^{63–68} indicate a larger effect of about 40–70%. In any case, quantum corrections to the diffusion constant quickly become less important at higher temperatures.⁶⁹ The calculated results remain a little below experiment up to 625 K, after which they become a little above experiment until right at the critical point where the 216 water simulation result agrees very well with experiment while the 512 water simulation result somewhat exceeds the experimental value.

The lower panel of Figure 4 shows the liquid self-diffusion constant versus pressure at the fixed supercritical temperature

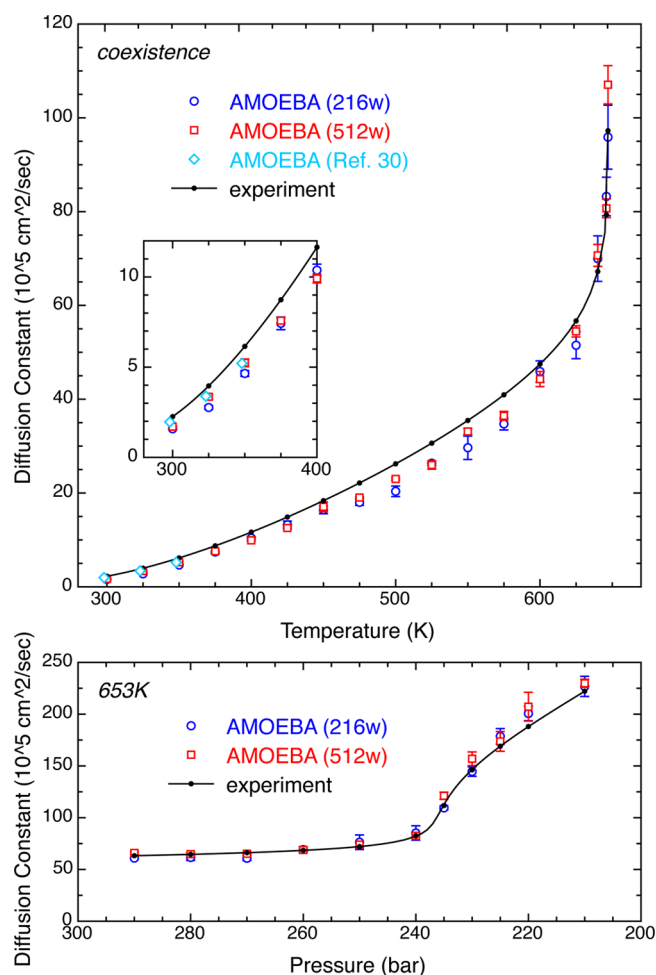


Figure 4. Self-diffusion constant of liquid vs temperature along the liquid–vapor coexistence line (upper panel) and vs pressure at fixed temperature of 653 K (lower panel).

of 653 K. The 216 and 512 water simulations agree very well with one another, and also agree well with experiment except for some slight overestimation at the lowest pressures.

Radial Distribution Functions. Radial distribution functions (RDFs) $g(r)$ for OO, OH, and HH are shown in Figure 5, all at densities corresponding to the liquid branch of the liquid–vapor coexistence line. The large spikes corresponding to short intramolecular OH and HH distances have been cut off for clarity. The AMOEBA results at ambient and high temperature are shown with red lines. Simulation results for 216 water boxes are indistinguishable from results for 512 water boxes on the scale of the figure, so only the latter are shown. Although not shown here for reasons of clarity, the previously determined¹⁶ AMOEBA RDFs at 298 K are also in excellent agreement with the present results. Experimental results at ambient temperature correspond to an analysis combining neutron and X-ray measurements with an empirical potential structure refinement procedure (EPSR)⁷⁰ (black lines) and, for OO, also correspond to X-ray diffraction measurements⁷¹ (green line). The two sets of experimental results at high temperature correspond to analyses combining neutron diffraction with EPSR taken with the same instrument on different days (solid and dashed black lines) to show the degree of experimental reproducibility.⁷²

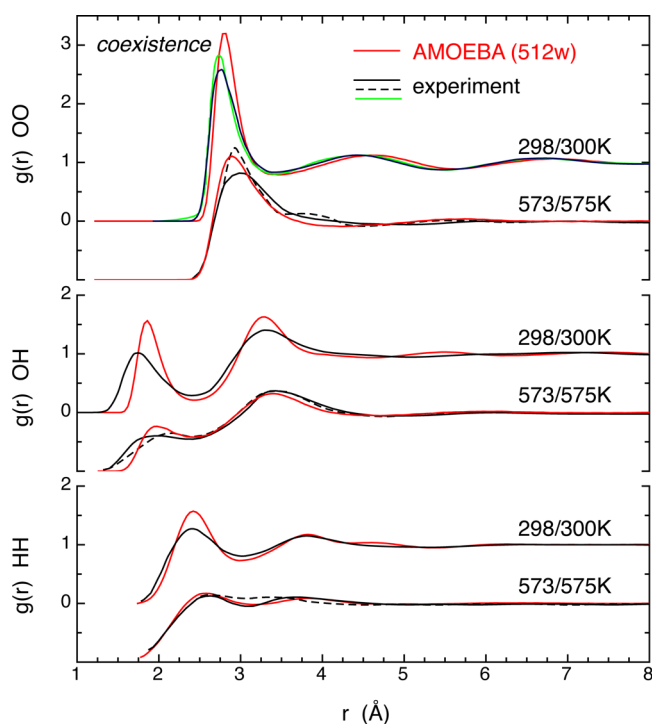


Figure 5. Radial distribution functions for OO (upper panel), OH (middle panel), and HH (lower panel). Experimental results at 298 and 573 K are compared to simulations at 300 and 575 K, respectively. The 573/575 K curves have been shifted down one unit for clarity.

The AMOEBA result for the first peak in the OO RDF at ~ 300 K lies at a slightly higher position and has higher amplitude than the experimental results shown. A recent EXAFS study⁷³ has indicated that this peak lies at slightly lower position and has significantly higher amplitude than found in most other experimental studies. However, a subsequent analysis⁷⁴ that considered both EXAFS and X-ray data simultaneously in the refinement found that this peak lies at about the same position but with somewhat lower amplitude than found in most other experimental studies. The first minimum, second peak, second minimum, and third peak in the AMOEBA curve all lie at slightly higher positions but essentially the same amplitudes as the two reported experimental curves.

The AMOEBA curve for the OH RDF at ~ 300 K has a first peak that is narrower and at somewhat higher position and amplitude than the experimental curve. The first minimum is in good agreement with experiment, and the second peak lies at nearly the same position but with slightly higher amplitude than the experiment.

The AMOEBA curve for the HH RDF at ~ 300 K has the first peak at slightly higher position than the experimental neutron curve, and is narrower and has higher amplitude. The remainder of the curve is in good agreement with experiment.

The AMOEBA curves for the OO, OH, and HH RDFs at ~ 575 K generally agree with the two experimental neutron diffraction results taken on different days to within the uncertainty suggested by the differences between those two.

Considering the uncertainty in the experimental results, as exemplified by the differences coming from various data sets and methods of analysis, it is concluded that the AMOEBA model provides a reasonable account of the RDFs at both ambient and high temperature.

Equilibrium Liquid–Gas Density. In this section we study the equilibrium liquid and gas densities, and from them the critical point parameters, that are characteristic of the AMOEBA model. For this purpose, the cubic box that was used in each of the previous sections, with size determined from the experimental density at the given temperature, was extended to be 3 times as large in the z direction in order to allow evaporation and consequent liquid–gas equilibrium. The number of molecules found in each of 200 bins slicing the extended z direction, as sampled and accumulated over each ps of a 1 ns run, then gave a profile of the equilibrium density as a function of z . At each temperature this profile was fit to the empirical functional form²¹

$$\rho(z) = \frac{(\rho_{\text{liq}} + \rho_{\text{gas}})}{2} - \frac{(\rho_{\text{liq}} - \rho_{\text{gas}})}{2} \operatorname{erf}\left(\frac{z - z_0}{\delta}\right)$$

where z_0 is the position of the Gibbs dividing surface and δ measures the interfacial thickness, in order to extract the liquid density ρ_{liq} and the gas density ρ_{gas} . The error function dependence was found to give slightly better fits than the alternatively sometimes used hyperbolic tangent.²¹

To clarify this procedure, representative data and fits at 475 K are given in Figure 6. The 216 and 512 water simulations

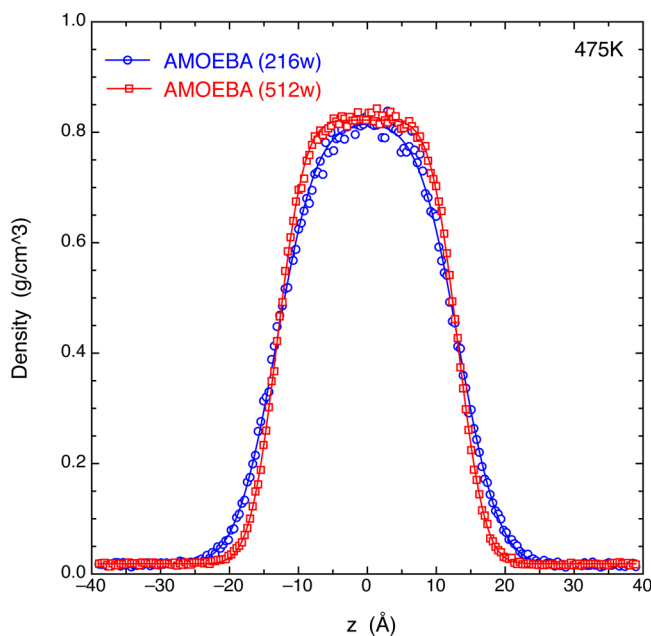


Figure 6. Density profile of the liquid–gas equilibrium from water simulation at 475 K. Points give the densities in bins slicing the extended z direction of the box, while the solid lines are fits using an empirical analytic function. The z -coordinate of the 216 water simulation has been artificially stretched in this plot by a factor of $(512/216)^{1/3} = 4/3$ to facilitate proper comparison with results from the larger box of the 512 water simulation.

each show a high-density liquid region in the center of the box, with gradual transitions over interfacial regimes to gaseous regions at either end of the box. While the two water simulations have somewhat different behavior in the interfacial regions, they agree well on the limiting fitted densities ρ_{liq} and ρ_{gas} . The analogous data and fits at other temperatures appeared reasonable up to 525 K, but at 550 K and above the plots showed interfacial regions comparable to the size of the simulation box and were therefore discarded as unreliable.

As a representative example to gauge convergence, the 1 ns trajectory of the 216 water simulation at 475 K was broken up into four segments of 250 ps each. The resulting liquid densities of 0.821, 0.827, 0.818, and 0.808 g/cm³ for the segments show a mean absolute deviation of only 0.006 g/cm³ from the full trajectory result of 0.817 g/cm³, and the resulting gas densities of 0.018, 0.016, 0.019, and 0.019 g/cm³ for the segments show a mean absolute deviation of only 0.001 g/cm³ from the full trajectory result of 0.017 g/cm³. The oscillations in the densities from the segments further suggest the absence of long-term drift in the results.

The results for ρ_{liq} and ρ_{gas} were then fitted to analytic functions of temperature based on the law of rectilinear diameters^{75,76} as extended to include a quadratic term²⁸

$$\frac{(\rho_{\text{liq}} + \rho_{\text{gas}})}{2} = \rho_c + C_1(T - T_c) + C_2(T - T_c)^2$$

together with the scaling law⁷⁷

$$\rho_{\text{liq}} - \rho_{\text{gas}} = C_3(T_c - T)^{0.3265}$$

Inclusion of the quadratic term in the first of these equations was found to produce substantial improvement in the fits. The universal critical exponent in the second of these equations is set to the accurate value recently determined for the Ising model.⁷⁸ The simplicity and small number of adjustable parameters in these equations suggest that they should not be expected to be reliable at temperatures far below the critical point. We therefore utilize simulation results for ρ_{liq} and ρ_{gas} only over the range 400–525 K for fitting to these equations.

Figure 7 shows the experimental, simulation, and fitted simulation results for the equilibrium liquid and gas densities as a function of temperature. Up to about 400 K the 216 and 512 water simulation results compare well with experiment, but as

temperature increases further the results from simulation show a significant underestimation of the liquid density and overestimation of the gas density.

The fits to the simulation densities as a function of temperature are extrapolated to higher temperatures in Figure 7 in order to estimate the behavior of the AMOEBA model where our simulations become unreliable for this purpose. The fits to the 216 and 512 water simulation results, respectively, give T_c of 591 and 597 K and ρ_c of 0.305 and 0.310 g/cm³. Comparing these gives an estimate of the possible error due to the finite size of the simulation boxes. To estimate the possible error due to the extrapolation procedure, we note that analogous fitting to the actual experimental liquid and gas densities at the same temperatures as used in analysis of the simulations predicts T_c to be 6 K above and ρ_c to be 0.006 g/cm³ below the actual experimental critical point parameters of 647.1 K and 0.322 g/cm³, respectively. Taking all these factors into account, we estimate the critical point parameters inherent to the AMOEBA model to be T_c of 597 ± 12 K, which is significantly below experiment, and ρ_c of 0.310 ± 0.011 g/cm³, which is very close to experiment. Significant underestimation of the critical temperature has also been found with most other water models,^{8,13,21,27–29} including various other polarizable water models.

We note that simulations become unphysical upon approaching very near to the critical point because the characteristic length scale of the fluctuations will then exceed the size of the simulation box. However, no indications of such a problem were apparent in any of the high-temperature cubic box simulations reported in the earlier sections of this work. The results in this section indicate the probable explanation is that use of experimental densities instead of model-determined densities kept those calculations sufficiently far away from the AMOEBA model's critical point to avoid such problems.

CONCLUSION

The AMOEBA model for water has been shown here to give a good account of the heat of vaporization, dielectric constant, self-diffusion constant, and radial distribution functions of water over a wide range from ambient to supercritical conditions when experimental densities are used. The calculated densities are also close to experiment near ambient conditions, but at high temperatures the liquid densities are underestimated and the gas densities are overestimated. As a consequence, the critical point of the model is reached at significantly too low temperature, although it occurs at approximately the correct density. Provided this limitation is kept in mind, it is concluded that the AMOEBA model should be very useful to describe the behavior of solutes in water from ambient to supercritical conditions.

AUTHOR INFORMATION

Notes

The authors declare no competing financial interest.

ACKNOWLEDGMENTS

Helpful discussions with Dr. J. D. Gezelter and Dr. J. Ponder are gratefully acknowledged. The research described herein was supported by the Division of Chemical Sciences, Geosciences and Biosciences, Basic Energy Sciences, Office of Science, United States Department of Energy, through grant no. DE-

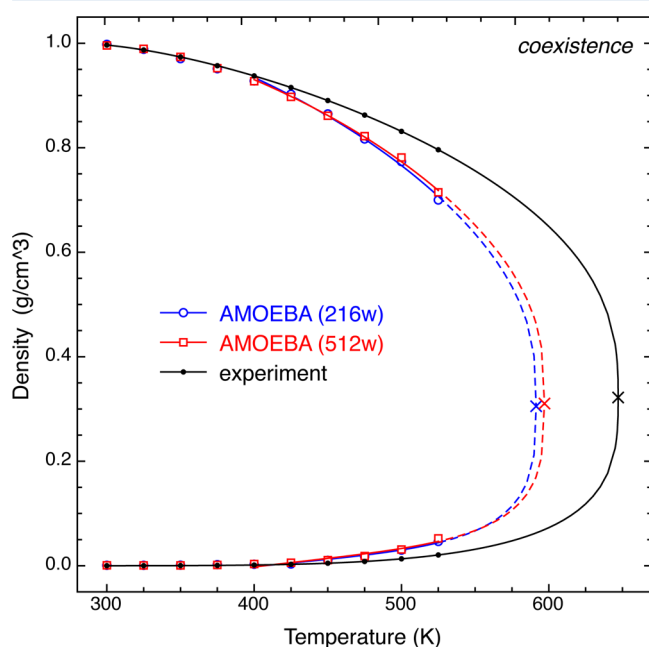


Figure 7. Equilibrium liquid and gas densities vs temperature along the liquid–vapor coexistence line. For the simulation results, solid lines give the fitted behavior in the temperature range used for the fitting, while dashed lines show extrapolations to higher temperatures. Critical points are marked with an × symbol.

FC02-04ER15533, This is contribution number NDRL-4955 from the Notre Dame Radiation Laboratory.

REFERENCES

- (1) Garrett, B. C.; Dixon, D. A.; Camaioni, D. M.; Chipman, D. M.; Johnson, M. A.; Jonah, C. D.; Kimmel, G. A.; Miller, J. H.; Rescigno, T. N.; Rossky, P. J.; et al. Role of water in electron-initiated processes and radical chemistry: Issues and scientific advances. *Chem. Rev.* **2005**, *105*, 355–389.
- (2) Elliot, A. J.; Bartels, D. M. *The Reaction Set, Rate Constants and g-Values for the Simulation of the Radiolysis of Light Water over the Range 20° to 350°C Based on Information Available in 2008*; Atomic Energy of Canada, Ltd., 2009.
- (3) Allinger, N. L.; Yuh, Y. H.; Li, J. H. Molecular Mechanics. The MM3 Force Field for Hydrocarbons. 1. *J. Am. Chem. Soc.* **1989**, *111*, 8551–8566.
- (4) Cornell, W. D.; Cieplak, P.; Bayly, C. I.; Gould, I. R.; Merz, K. M.; Ferguson, D. M.; Spellmeyer, D. C.; Fox, T.; Caldwell, J. W.; Kollman, P. A. A Second Generation Force Field for the Simulation of Proteins, Nucleic Acids, and Organic Molecules. *J. Am. Chem. Soc.* **1995**, *117*, 5179–5197.
- (5) Jorgensen, W. L.; Maxwell, D. S.; Tirado-Rives, J. Development and Testing of the OPLS All-Atom Force Field on Conformational Energetics and Properties of Organic Liquids. *J. Am. Chem. Soc.* **1996**, *118*, 11225–11236.
- (6) MacKerell, A. D.; Bashford, D.; Bellott, M.; Dunbrack, R. L.; Evanseck, J. D.; Field, M. J.; Fischer, S.; Gao, J.; Guo, H.; Ha, S.; et al. All-atom empirical potential for molecular modeling and dynamics studies of proteins. *J. Phys. Chem. B* **1998**, *102*, 3586–3616.
- (7) Oostenbrink, C.; Villa, A.; Mark, A. E.; Van Gunsteren, W. F. Molecular force field based on the free enthalpy of hydration and solvation: The GROMOS force-field parameter sets 53A5 and 53A6. *J. Comput. Chem.* **2004**, *25*, 1656–1676.
- (8) Guillot, B. A reappraisal of what we have learnt during three decades of computer simulations on water. *J. Mol. Liq.* **2002**, *101*, 219–260.
- (9) Bernardo, D. N.; Ding, Y. B.; Krogh-Jespersen, K.; Levy, R. M. An Anisotropic Polarizable Water Model: Incorporation of All-Atom Polarizabilities into Molecular Mechanics Force Fields. *J. Phys. Chem.* **1994**, *98*, 4180–4187.
- (10) Rick, S. W.; Stuart, S. J.; Berne, B. J. Dynamical fluctuating charge force fields: Application to liquid water. *J. Chem. Phys.* **1994**, *101*, 6141–6156.
- (11) Dang, L. X.; Chang, T.-M. Molecular dynamics study of water clusters, liquid, and liquid-vapor interface of water with many-body potentials. *J. Chem. Phys.* **1997**, *106*, 8149–8159.
- (12) Bursulaya, B. D.; Jeon, J.; Zichi, D. A.; Kim, H. J. Generalized molecular mechanics including quantum electronic structure variation of polar solvents. II. A molecular dynamics simulation study of water. *J. Chem. Phys.* **1998**, *108*, 3286–3295.
- (13) Chen, B.; Xing, J. H.; Siepmann, J. I. Development of polarizable water force fields for phase equilibrium calculations. *J. Phys. Chem. B* **2000**, *104*, 2391–2401.
- (14) Jeon, J.; Lefohn, A. E.; Voth, G. A. An improved Polarflex water model. *J. Chem. Phys.* **2003**, *118*, 7504–7518.
- (15) Lamoureux, G.; MacKerell, A. D., Jr.; Roux, B. A simple polarizable model of water based on classical Drude oscillators. *J. Chem. Phys.* **2003**, *119*, 5185–5197.
- (16) Ren, P.; Ponder, J. W. Polarizable atomic multipole water model for molecular mechanics simulation. *J. Phys. Chem. B* **2003**, *107*, 5933–5947.
- (17) Yu, H. B.; van Gunsteren, W. F. Charge-on-spring polarizable water models revisited: From water clusters to liquid water to ice. *J. Chem. Phys.* **2004**, *121*, 9549–9564.
- (18) Paricaud, P.; Predota, M.; Chialvo, A. A.; Cummings, P. T. From dimer to condensed phases at extreme conditions: Accurate predictions of the properties of water by a Gaussian charge polarizable model. *J. Chem. Phys.* **2005**, *122*, 244511:1–14.
- (19) Bukowski, R.; Szalewicz, K.; Groenenboom, G. C.; van der Avoird, A. Predictions of the properties of water from first principles. *Science* **2007**, *315*, 1249–1252.
- (20) Fanourgakis, G. S.; Xantheas, S. S. Development of transferable interaction potentials for water. V. Extension of the flexible, polarizable, Thole-type model potential (TTM3-F, v. 3.0) to describe the vibrational spectra of water clusters and liquid water. *J. Chem. Phys.* **2008**, *128*, 074506:1–11.
- (21) Bauer, B. A.; Patel, S. Properties of water along the liquid-vapor coexistence curve via molecular dynamics simulations using the polarizable TIP4P-QDP-LJ water model. *J. Chem. Phys.* **2009**, *131*, 084709:1–16.
- (22) Kumar, R.; Wang, F.-F.; Jenness, G. R.; Jordan, K. D. A second generation distributed point polarizable water model. *J. Chem. Phys.* **2010**, *132*, 014309:1–12.
- (23) Omololu, A.-O.; Szalewicz, K. How well can polarization models of pairwise nonadditive forces describe liquid water? *J. Chem. Phys.* **2013**, *138*, 024316:1–13.
- (24) Kumar, R.; Skinner, J. L. Water simulation model with explicit three-molecule interactions. *J. Phys. Chem. B* **2008**, *112*, 8311–8318.
- (25) Tainter, C. J.; Pieniazek, P. A.; Lin, Y.-S.; Skinner, J. L. Robust three-body water simulation model. *J. Chem. Phys.* **2011**, *134*, 184501:1–10.
- (26) Babin, V.; Medders, G. R.; Paesani, F. Toward a Universal Water Model: First Principles Simulations from the Dimer to the Liquid Phase. *J. Phys. Chem. Lett.* **2012**, *3*, 3765–3769.
- (27) Kiyohara, K.; Gubbins, K. E.; Panagiotopoulos, A. Z. Phase coexistence properties of polarizable water models. *Mol. Phys.* **1998**, *94*, 803–808.
- (28) Yezdimer, E. M.; Cummings, P. T. Calculation of the vapour-liquid coexistence curve for a fluctuating point charge water model. *Mol. Phys.* **1999**, *97*, 993–996.
- (29) Dang, L. X.; Chang, T. M.; Panagiotopoulos, A. Z. Gibbs ensemble Monte Carlo simulations of coexistence properties of a polarizable potential model of water. *J. Chem. Phys.* **2002**, *117*, 3522–3523.
- (30) Ren, P. Y.; Ponder, J. W. Temperature and pressure dependence of the AMOEBA water model. *J. Phys. Chem. B* **2004**, *108*, 13427–13437.
- (31) Benjamin, K. M.; Schultz, A. J.; Kofke, D. A. Virial coefficients of polarizable water: Applications to thermodynamic properties and molecular clustering. *J. Phys. Chem. C* **2007**, *111*, 16021–16027.
- (32) Benjamin, K. M.; Schultz, A. J.; Kofke, D. A. Fourth and Fifth Virial Coefficients of Polarizable Water. *J. Phys. Chem. B* **2009**, *113*, 7810–7815.
- (33) Chialvo, A. A.; Horita, J. Liquid-vapor equilibrium isotopic fractionation of water: How well can classical water models predict it? *J. Chem. Phys.* **2009**, *130*, 094509:1–12.
- (34) Chialvo, A. A.; Horita, J. Polarization behavior of water in extreme aqueous environments: A molecular dynamics study based on the Gaussian charge polarizable water model. *J. Chem. Phys.* **2010**, *133*, 074504:1–10.
- (35) Ponder, J. W.; Wu, C.; Ren, P.; Pande, V. S.; Chodera, J. D.; Schnieders, M. J.; Haque, I.; Mobley, D. L.; Lambrecht, D. S.; DiStasio, R. A., Jr.; et al. Current Status of the AMOEBA Polarizable Force Field. *J. Phys. Chem. B* **2010**, *114*, 2549–2564.
- (36) Ren, P.; Wu, C.; Ponder, J. W. Polarizable Atomic Multipole-Based Molecular Mechanics for Organic Molecules. *J. Chem. Theor. Comput.* **2011**, *7*, 3143–3161.
- (37) Shi, Y.; Wu, C.; Ponder, J. W.; Ren, P. Multipole Electrostatics in Hydration Free Energy Calculations. *J. Comput. Chem.* **2011**, *32*, 967–977.
- (38) Grossfield, A.; Ren, P.; Ponder, J. W. Ion solvation thermodynamics from simulation with a polarizable force field. *J. Am. Chem. Soc.* **2003**, *125*, 15671–15682.
- (39) Grossfield, A. Dependence of ion hydration on the sign of the ion's charge. *J. Chem. Phys.* **2005**, *122*, 024506:1–10.

- (40) Jiao, D.; King, C.; Grossfield, A.; Darden, T. A.; Ren, P. Simulation of Ca^{2+} and Mg^{2+} solvation using polarizable atomic multipole potential. *J. Phys. Chem. B* **2006**, *110*, 18553–18559.
- (41) Piquemal, J.-P.; Perera, L.; Cisneros, G. A.; Ren, P.; Pedersen, L. G.; Darden, T. A. Towards accurate solvation dynamics of divalent cations in water using the polarizable amoeba force field: From energetics to structure. *J. Chem. Phys.* **2006**, *125*, 054511:1–7.
- (42) Rogers, D. M.; Beck, T. L. Quasichemical and structural analysis of polarizable anion hydration. *J. Chem. Phys.* **2010**, *132*, 014505:1–12.
- (43) Wu, J. C.; Piquemal, J.-P.; Chaudret, R.; Reinhardt, P.; Ren, P. Polarizable Molecular Dynamics Simulation of $\text{Zn}(\text{II})$ in Water Using the AMOEBA Force Field. *J. Chem. Theor. Comput.* **2010**, *6*, 2059–2070.
- (44) Zhao, Z.; Rogers, D. M.; Beck, T. L. Polarization and charge transfer in the hydration of chloride ions. *J. Chem. Phys.* **2010**, *132*, 014502:1–10.
- (45) Medders, G. R.; Babin, V.; Paesani, F. A Critical Assessment of Two-Body and Three-Body Interactions in Water. *J. Chem. Theor. Comput.* **2013**, *9*, 1103–1114.
- (46) Thole, B. T. Molecular Polarizabilities Calculated with a Modified Dipole Interaction. *Chem. Phys.* **1981**, *59*, 341–350.
- (47) Ponder, J. W. *TINKER: Software Tools for Molecular Design, Version 4.2*; Washington University School of Medicine: Saint Louis, MO, 2004.
- (48) Berendsen, H. J. C.; Postma, J. P. M.; van Gunsteren, W. F.; Dinola, A.; Haak, J. R. Molecular Dynamics with Coupling to an External Bath. *J. Chem. Phys.* **1984**, *81*, 3684–3690.
- (49) Morishita, T. Fluctuation formulas in molecular-dynamics simulations with the weak coupling heat bath. *J. Chem. Phys.* **2000**, *113*, 2976–2982.
- (50) Beeman, D. Some Multistep Methods for use in Molecular Dynamics Calculations. *J. Comp Phys.* **1976**, *20*, 130–139.
- (51) Brooks, B. R. *Algorithms for Molecular Dynamics at Constant Temperature and Pressure*; National Institutes of Health: Bethesda, MD, 1988.
- (52) Wagner, W.; Pruss, A. The IAPWS formulation 1995 for the thermodynamic properties of ordinary water substance for general and scientific use. *J. Phys. Chem. Ref. Data* **2002**, *31*, 387–535.
- (53) NIST—ASME Steam Properties Database, Version 2.22, 2008.
- (54) Burnham, C. J.; Xantheas, S. S. On the importance of zero-point effects in molecular level classical simulations of water. *J. Mol. Liq.* **2004**, *110*, 177–192.
- (55) Neumann, M. Dipole moment fluctuation formulas in computer simulations of polar systems. *Mol. Phys.* **1983**, *50*, 841–858.
- (56) Neumann, M.; Steinhauser, O. Computer simulation and the dielectric constant of polarizable polar systems. *Chem. Phys. Lett.* **1984**, *106*, 563–569.
- (57) Burnham, C. J.; Anick, D. J.; Mankoo, P. K.; Reiter, G. F. The vibrational proton potential in bulk liquid water and ice. *J. Chem. Phys.* **2008**, *128*, 154519:1–20.
- (58) Flyvbjerg, H.; Petersen, H. G. Error Estimates on Averages of Correlated Data. *J. Chem. Phys.* **1989**, *91*, 461–466.
- (59) Wu, Y. J.; Tepper, H. L.; Voth, G. A. Flexible simple point-charge water model with improved liquid-state properties. *J. Chem. Phys.* **2006**, *124*, 024503:1–12.
- (60) Yoshida, K.; Matubayasi, N.; Uosaki, Y.; Nakahara, M. Scaled Polynomial Expression for Self-Diffusion Coefficients for Water, Benzene, and Cyclohexane over a Wide Range of Temperatures and Densities. *J. Chem. Eng. Data* **2010**, *55*, 2815–2823.
- (61) Habershon, S.; Markland, T. E.; Manolopoulos, D. E. Competing quantum effects in the dynamics of a flexible water model. *J. Chem. Phys.* **2009**, *131*, 024501:1–11.
- (62) Liu, J.; Miller, W. H.; Paesani, F.; Zhang, W.; Case, D. A. Quantum dynamical effects in liquid water: A semiclassical study on the diffusion and the infrared absorption spectrum. *J. Chem. Phys.* **2009**, *131*, 164509:1–12.
- (63) Lobaugh, J.; Voth, G. A. A quantum model for water: Equilibrium and dynamical properties. *J. Chem. Phys.* **1997**, *106*, 2400–2410.
- (64) de la Pena, L. H.; Kusalik, P. G. Quantum effects in light and heavy liquid water: A rigid-body centroid molecular dynamics study. *J. Chem. Phys.* **2004**, *121*, 5992–6002.
- (65) Miller, T. F.; Manolopoulos, D. E. Quantum diffusion in liquid water from ring polymer molecular dynamics. *J. Chem. Phys.* **2005**, *123*, 154504:1–10.
- (66) Paesani, F.; Zhang, W.; Case, D. A.; Cheatham, T. E., III; Voth, G. A. An accurate and simple quantum model for liquid water. *J. Chem. Phys.* **2006**, *125*, 184507:1–11.
- (67) Paesani, F.; Iuchi, S.; Voth, G. A. Quantum effects in liquid water from an ab initio-based polarizable force field. *J. Chem. Phys.* **2007**, *127*, 074506:1–15.
- (68) Zeidler, A.; Salmon, P. S.; Fischer, H. E.; Neufeind, J. C.; Simonson, J. M.; Markland, T. E. Isotope effects in water as investigated by neutron diffraction and path integral molecular dynamics. *J. Phys.: Condens. Matter* **2012**, *24*, 284126:1–13.
- (69) de la Pena, L. H.; Kusalik, P. G. Temperature dependence of quantum effects in liquid water. *J. Am. Chem. Soc.* **2005**, *127*, 5246–5251.
- (70) Soper, A. K.; Benmore, C. J. Quantum differences between heavy and light water. *Phys. Rev. Lett.* **2008**, *101*, 065502:1–4.
- (71) Sorenson, J. M.; Hura, G.; Glaeser, R. M.; Head-Gordon, T. What can x-ray scattering tell us about the radial distribution functions of water? *J. Chem. Phys.* **2000**, *113*, 9149–9161.
- (72) Soper, A. K. The radial distribution functions of water and ice from 220 to 673 K and at pressures up to 400 MPa. *Chem. Phys.* **2000**, *258*, 121–137.
- (73) Bergmann, U.; Di Cicco, A.; Wernet, P.; Principi, E.; Glatzel, P.; Nilsson, A. Nearest-neighbor oxygen distances in liquid water and ice observed by x-ray Raman based extended x-ray absorption fine structure. *J. Chem. Phys.* **2007**, *127*, 174504:1–5.
- (74) Wikfeldt, K. T.; Leetmaa, M.; Mace, A.; Nilsson, A.; Pettersson, L. G. M. Oxygen-oxygen correlations in liquid water: Addressing the discrepancy between diffraction and extended x-ray absorption fine-structure using a novel multiple-data set fitting technique. *J. Chem. Phys.* **2010**, *132*, 104513:1–10.
- (75) Rowlinson, J. S.; Swinton, F. L. *Liquids and Liquid Mixtures*, 3rd ed.; Butterworth: London, 1982.
- (76) Frenkel, D.; Smit, B. *Understanding Molecular Simulation. From Algorithms to Applications*; Academic Press: London, 2002.
- (77) Rowlinson, J. S.; Widom, B. *Molecular Theory of Capillarity*; Clarendon Press: Oxford, UK, 1982.
- (78) Campostrini, M.; Pelissetto, A.; Rossi, P.; Vicari, E. 25th-order high-temperature expansion results for three-dimensional Ising-like systems on the simple-cubic lattice. *Phys. Rev. E* **2002**, *65*, 066127:1–19.